NASA TECHNICAL NOTE

NASA TN D-4846

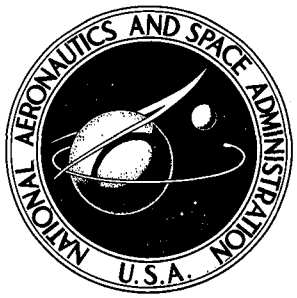

NASA TN D-4846

ANALYSIS OF THE AEROELASTIC DIVERGENCE OF TWO EXPERIMENTAL UNGUIDED LAUNCH VEHICLES

by Clarence P. Young, Jr.

Langley Research Center

Langley Station, Hampton, Va.

NATIONAL AERONAUTICS AND SPACE ADMINISTRATION • WASHINGTON, D. C. • NOVEMBER 1968

NASA TN D-4846

ANALYSIS OF THE AEROELASTIC DIVERGENCE OF TWO EXPERIMENTAL UNGUIDED LAUNCH VEHICLES

By Clarence P. Young, Jr.

Langley Research Center
Langley Station, Hampton, Va.

NATIONAL AERONAUTICS AND SPACE ADMINISTRATION

For sale by the Clearinghouse for Federal Scientific and Technical Information
Springfield, Virginia 22151 – CFSTI price $3.00

ANALYSIS OF THE AEROELASTIC DIVERGENCE OF TWO EXPERIMENTAL UNGUIDED LAUNCH VEHICLES

By Clarence P. Young, Jr.
Langley Research Center

SUMMARY

A theoretical analysis of two experimental launch vehicles which are known to have failed because of aeroelastic divergence is presented. Data for the analysis and the calculated aeroelastic divergence characteristics are provided. The analytical results and the flight results of the two divergent vehicles are compared. The correlation of the analytical predictions with the actual flight behavior is used for evaluating the method of analysis and to explore further the aeroelastic divergence phenomenon in unguided launch vehicles.

INTRODUCTION

The phenomenon of aeroelastic divergence is recognized to be of primary importance in the design of high performance, highly flexible launch vehicles. It is characterized by an unstable flight condition arising from the adverse interaction of aerodynamic forces and elastic deformation of the vehicle structure. The evaluation of the launch-vehicle design in view of its aeroelastic divergence characteristics requires a theoretical analysis which must be adequate for predicting this divergence behavior. Thus, investigations which correlate theoretical predictions of aeroelastic divergence with that observed from experiment or actual flight are important to the development of acceptable theories.

The amount of available documented data on aeroelastic divergence failures of launch vehicles is limited. Most aeroelastic investigations in the past have been concerned with the experimental and analytical investigations of low-aspect-ratio wings and control surfaces. However, experimental and analytical research on the slender-launch-vehicle divergence phenomena is needed to evaluate existing and newly developed theories and to explore the dynamic aspects of divergence behavior.

Correlations of theoretical predictions of aeroelastic divergence with aeroelastic divergence failures observed during flight are documented in references 1 and 2. In reference 1, theoretical and experimental correlations were obtained from flights of

several small model-booster rocket configurations. The investigations of reference 1 showed that a successful flight was usually obtained if the analysis predicted the simplified model-booster combinations to be "safe." However, the method of reference 1 does not directly yield stability roots and does not conveniently lend itself to the analysis of larger, more complex, multistage vehicle structures; thus, predictions of divergence by this method would, in all likelihood, be less accurate.

The aeroelastic divergence failures of two experimental two-stage launch vehicles are documented in reference 2 along with a theoretical analysis of the failures. The theory presented in reference 2 gave conservative results (that is, early divergence is predicted) when compared with the two flight failures. However, the analytical technique of reference 2 was found to be useful in explaining the mode of failure of the two launch vehicles.

The documentation of the aeroelastic divergence failures in reference 2 provided an opportunity to analyze the failures by the method of reference 3, which is currently used at the Langley Research Center for the aeroelastic design evaluation of unguided slender-body launch vehicles. The additional data necessary for the present analysis were obtained from the Weapons Research Establishment of the Australian Department of Supply. These data provided a source of information on flight divergence and subsequent failures that could then be used to evaluate the theory of reference 3.

This paper presents a correlation of the analytical predictions of aeroelastic divergence behavior with the actual flight behavior of two experimental launch vehicles known to have failed because of aeroelastic divergence. The objectives of the investigation are to evaluate the adequacy of the method of reference 3 to predict aeroelastic divergence and to gain further insight into the divergence phenomenon.

The NASA Langley Research Center is indebted to the Weapons Research Establishment for their cooperation in supplying the information necessary to this study.

SYMBOLS

The units of measure used in the applied analysis are in the U.S. Customary System. However, alternate values are provided in the International System (SI) to increase the usefulness of the paper. Details of the SI system and necessary conversion factors are available in reference 4.

b semispan of exposed fin, in. (m)

$\left(C_{L_\alpha} S\right)_{F,B}$ product of fin-body-combination lift-force-coefficient slope and fin reference area, in^2/rad (m^2/rad)

c_r chord of fin at fin-body juncture, in. (m)

c_t tip chord of fin, in. (m)

D mean body diameter of first stage of two-stage configuration, in. (m)

E modulus of elasticity of vehicle in bending, lbf/in^2 (N/m^2)

EI flexural stiffness, $lbf\text{-}in^2$ $(N\text{-}m^2)$

I area moment of inertia of a cross section, in^4 (m^4)

$K_{B(W)}$ ratio of lift of body (of fin-body combination) to lift of an isolated fin

$K_{W(B)}$ ratio of lift of fin (of fin-body combination) to lift of an isolated fin

L total length of vehicle, in. (m)

m distributed mass of vehicle, $lbf\text{-}sec^2/in^2$ $(N\text{-}sec^2/m^2)$

q flight dynamic pressure, $\frac{1}{2}\rho u^2$, lbf/in^2 (N/m^2)

q_{div} dynamic pressure of divergence, lbf/in^2 (N/m^2)

R radius of curvature of flight path at $x = 0$, in. (m)

S characteristic reference area, in^2 (m^2)

$S\frac{dC_D}{dx}$ product of associated reference area and distributed forebody drag-force-coefficient slope, in. (m)

$S\frac{dC_{L_\alpha}}{dx}$ product of associated reference area and distributed lift-force-coefficient slope, in./rad (m/rad)

t flight time, sec

u	velocity of vehicle, tangent to flight path at $x = 0$, in./sec (m/sec)
X,Y	system axes
x	independent coordinate along length of vehicle, taken tangent to flight path at $x = 0$, in. (m)
x_{cg}	coordinate to center of gravity, in. (m)
x_{cp}	coordinate to aerodynamic center of pressure of rigid vehicle, in. (m)
x_{gsm}	generalized static margin (see eq. (23), ref. 5), in. (m)
$x_{sm,rig}$	rigid-vehicle static margin, $x_{cg} - x_{cp}$, in. (m)
y	elastic deformation of vehicle measured relative to X-axis, in. (m)
α	local angle of attack, rad
α_o	angle of attack at $x = 0$, rad
κ_u	estimated local rotational increment at $x = x_u$ due to joint flexibility, rad/in-lbf (rad/m-N)
ρ	air density, lbf-sec^2/in^4 (N-sec^2/m^4)
Λ_{le}	sweep angle of fin leading edge, deg (rad)

Subscripts:

ref	reference value
u	coordinate of uth joint

METHOD OF ANALYSIS

The theoretical method of analysis used in the present investigation is described in reference 3. The analysis is a rigorous mathematical approach to the problem of launch-vehicle divergence and has been used extensively at the Langley Research Center (LRC) for expediting and evaluating launch-vehicle design.

The method utilizes a matrix recurrence solution to the system differential equations, which describe static aeroelastic behavior, and it yields the stability boundary at which aeroelastic divergence will occur. It is directly applicable to a continuous system representation and accurately accommodates axial discontinuities in both input and output characteristics. Secondary influences of thrust and aerodynamic cross flow are incorporated.

Measures of Aeroelastic Stability

The principal measure of stability for the flexible vehicle that is used in the present paper is the ratio of the vehicle flight dynamic pressure to the theoretical dynamic pressure of divergence q/q_{div}. The divergence dynamic pressure is defined as the dynamic pressure beyond which divergent flight behavior will occur because of aeroelastic instability.

Another measure of aeroelastic stability used herein is the generalized static margin, which approximately accounts for the departure from the rigid-vehicle static margin because of aeroelastic effects. The generalized static margin is computed by the method given in reference 5.

A discussion of these measures of aeroelastic stability and their significance when employed in the design and evaluation of unguided launch vehicles can be found in references 3 and 5.

Theoretical Considerations

This section is devoted to a description of the procedure for establishing the theoretical condition of divergence, along with some comments on transient behavior.

Theoretical prediction of aeroelastic divergence.- The theoretically predicted divergence condition occurs at the point on the trajectory beyond which the vehicle becomes unstable because of aeroelastic effects. This condition is defined in the analysis as the point at which the actual flight dynamic pressure is equal to the calculated dynamic pressure of divergence.

The stability boundary or divergence dynamic pressure q_{div} that is computed in the analysis identifies the state of neutral stability for the flexible vehicle at a particular condition associated with a particular combination of system parameters. Since the primary purpose of the present paper is to show correlation between computed and observed results of aeroelastic divergence, a rigorous iterative procedure, which is described in detail in references 3 and 5, was used to determine the point on the actual trajectory at which the condition of theoretical aeroelastic divergence is predicted.

Transient behavior.- The static methods of analysis cannot account for the transient behavior of the vehicle in the divergent mode. The analysis assumes an instantaneous aeroelastic response of the system, which is assumed to be characterized by a nonoscillatory equilibrium condition at a particular time along the trajectory.

The complete timewise response of the elastic vehicle would have to be examined by a dynamic program. However, for the nonspinning vehicle in the absence of large atmospheric disturbances, the steady-state divergence prediction should agree very closely with dynamic predictions. In most cases, the excitation frequencies for the elastic, nonrolling vehicle that would bring into play the dynamic oscillatory inertial loadings are well removed from the low-frequency disturbances normally encountered in flight. Thus, static methods are considered to be appropriate and are, in fact, widely used in the aeroelastic analysis of launch vehicles.

VEHICLES DESCRIPTION AND FLIGHT BEHAVIOR

Configurations

Two launch vehicles (designated A and B) are analyzed. A configuration sketch applicable to both vehicles is given in figure 1. The principal difference between vehicles A and B was that the second stage of vehicle B was stiffened by the addition of a steel sleeve over the entire length of the second-stage motor.

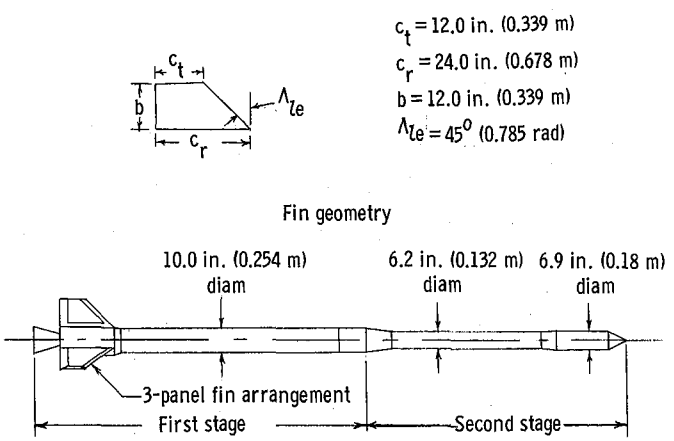

Figure 1.- Configuration and fin geometry of vehicles A and B.

Vehicles A and B were unguided two-stage experimental launch vehicles designed for a no-roll flight. Both vehicles were stabilized during first-stage flight by identical

three-panel fin arrangements, and the second stage was flare stabilized. A sketch of the fin-panel geometry is also given in figure 1. More detailed information on the vehicle configurations can be found in references 2 and 6. The vehicle designations used in this investigation correspond to those used in reference 2.

Flight Divergence Behavior

The aeroelastic divergence failures of launch vehicles A and B are described in reference 2. Both vehicles failed prior to first-stage burnout. Camera and telemetry records verified that the vehicles flew satisfactorily during the first few seconds of flight. The divergence behavior of both vehicles was characterized by a sudden, rapid buildup in lateral accelerations followed by structural failure in which, as stated in reference 2, the instrumentation head of each vehicle broke off. Vehicle A failed at 2.5 seconds after launch (Mach 3.05) at a dynamic pressure of approximately 12 750 lb/ft^2 (610 473 N/m^2). Vehicle B failed at 3.15 seconds after launch (Mach 4.04) at a dynamic pressure of approximately 21 980 lb/ft^2 (1 052 408 N/m^2).

Normal and lateral accelerometer data indicate a rapid aeroelastic response. For vehicle A, telemetry records indicate a time lapse of approximately 0.08 second from onset of divergence to actual failure. The telemetry data for vehicle B indicate a time lapse of approximately 0.14 second from the onset of divergence to actual failure. The divergence behavior is assumed to begin when the lateral accelerations observed from the flight records began to diverge from the undisturbed flight condition. These data are useful to identify the onset of aeroelastic divergence; however, theoretical predictions are correlated with the actual aforementioned failure times.

RESULTS AND DISCUSSION

This section begins with a discussion of the input data used in the applied analysis. The input data include the mass and stiffness characteristics and data that were used to verify structural stiffness computations. Other input data include the trajectory parameters and the aerodynamic lift and drag characteristics. Another topic discussed in this section is the correlation of computed aeroelastic divergence characteristics with flight results. The computed divergence characteristics include the divergence boundaries, aeroelastic stability measures, and the divergence mode shapes. In addition, the static stability data based upon a rigid-body assumption are discussed and the method of analysis is evaluated in view of the present correlations as well as past experience with application of the method.

Input Data

The aeroelastic analyses input data provided by the Weapons Research Establishment (WRE) include mass distributions, detailed drawings, trajectory data, and supplementary aerodynamic data.

Mass data.- The mass distributions furnished for vehicles A and B for the pre-launch configurations are given in table I. These data (along with the distributions at failure) are illustrated graphically in figure 2. The axial discontinuities observed in the mass per inch curves of figure 2 are accounted for in table I by recording both quantities for their common x/L value.

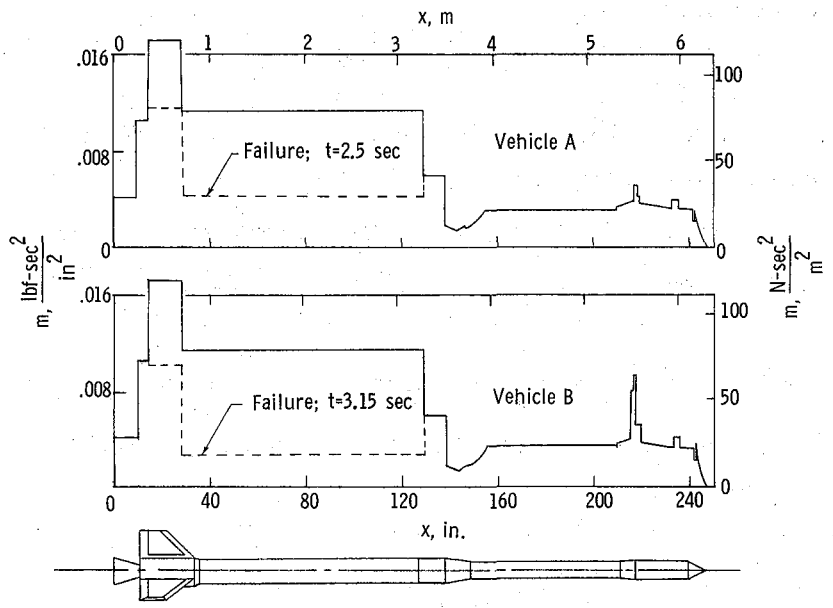

Figure 2.- Mass distributions prior to launch and at failure for vehicles A and B.

The mass distributions in figure 2 are adjusted in the analysis at times during first-stage boost to account for the loss of expended fuel. The timewise variations in the computed weights and centers of gravity obtained for the adjusted mass distributions for both vehicles agree closely with those given in references 2 and 6.

Stiffness data.- The flexural stiffness distributions were computed from the vehicle drawings provided by WRE. These data are presented in table II and are shown graphically in figure 3 for both vehicles. The discontinuities in the curves of figure 3 are accounted for in table II in the manner previously mentioned for the mass quantities in table I.

TABLE I.- MASS DISTRIBUTION PRIOR TO LAUNCH FOR VEHICLES A AND B

[m_{ref} = 1.0 lbf-sec^2/in^2 (6894.76 N-sec^2/m^2); L = 248.0 in. (6.299 m)]

x/L	m/m_{ref} (a)		x/L	m/m_{ref} (a)	
	Vehicle A	Vehicle B		Vehicle A	Vehicle B
0	0.0041	0.0041	0.8515	0.0033	0.0037
.0395	.0041	.0041	.8717	.0038	.0041
.0395	.0109	.0109	.8810	.0039	.0043
.0605	.0109	.0109	.8810	.0052	.0056
.0605	.0172	.0172	.8850	.0052	.0052
.1169	.0172	.0172	.8850	.0042	.0042
.1169	.0113	.0113	.8891	.0042	.0042
.5242	.0113	.0113	.8891	.0037	.0037
.5242	.0060	.0060	.8899	.0037	.0037
.5604	.0060	.0060	.8919	.0036	.0036
.5604	.0018	.0018	.8935	.0036	.0036
.5629	.0016	.0016	.8955	.0036	.0036
.5649	.0018	.0018	.9157	.0033	.0033
.5669	.0014	.0014	.9435	.0033	.0033
.5681	.0015	.0015	.9435	.0039	.0039
.5697	.0016	.0016	.9536	.0039	.0039
.5826	.0014	.0014	.9536	.0032	.0032
.5863	.0017	.0017	.9778	.0032	.0032
.5988	.0016	.0016	.9778	.0012	.0012
.6045	.0018	.0018	.9818	.0012	.0012
.6086	.0020	.0020	.9818	.0029	.0029
.6113	.0021	.0021	.9868	.0016	.0016
.6229	.0025	.0029	.9878	.0011	.0011
.6235	.0028	.0032	.9890	.0010	.0010
.6310	.0031	.0035	.9925	.0007	.0007
.8508	.0031	.0035	.9961	.0002	.0002
.8508	.0033	.0035	1.0000	0	0

[a]Points of discontinuity in the m/m_{ref} function are recorded for their common x/L values.

TABLE II.- FLEXURAL STIFFNESS DISTRIBUTION FOR LAUNCH VEHICLES A AND B

[$(EI)_{ref}$ = 10 × 10^9 lbf-in^2 (0.0287 × 10^9 N-m^2); L = 248.0 in. (6.299 m)]

x/L	EI/EI_{ref} (a)		x/L	EI/EI_{ref} (a)		x/L	EI/EI_{ref} (a)	
	Vehicle A	Vehicle B		Vehicle A	Vehicle B		Vehicle A	Vehicle B
0	0.1527	0.1527	0.6086	0.0218	0.0218	0.9309	0.0042	0.0103
.0300	.0626	.0626	.6113	.0290	.0290	.9326	.0043	.0103
.0300	.2851	.2851	.6113	.0302	.0383	.9407	.0044	.0101
.0472	.3120	.3120	.6229	.0157	.0248	.9435	.0046	.0099
.0536	.3346	.3346	.6235	.0152	.0244	.9501	.0047	.0098
.0536	.0338	.0338	.6310	.0151	.0242	.9501	.0011	.0011
.0681	.0338	.0338	.6333	.0150	.0241	.9548	.0011	.0011
.0681	.0746	.0746	.6352	.0224	.0315	.9548	.1920	.1924
.5181	.0746	.0746	.6352	.0051	.0053	.9568	.1920	.1924
.5242	.1040	.1040	.6376	.0051	.0053	.9568	.0279	.0338
.5250	.1040	.1040	.6376	.0273	.0364	.9608	.0279	.0338
.5250	.0029	.0029	.6380	.0298	.0389	.9608	.0052	.0111
.5371	.0029	.0029	.6398	.0177	.0268	.9632	.0051	.0111
.5371	.3926	.3926	.6414	.0201	.0292	.9754	.0046	.0111
.5375	.3926	.3926	.6428	.0066	.0159	.9778	.0045	.0111
.5536	.0659	.0659	.8838	.0066	.0159	.9810	.0033	.0111
.5649	.0659	.0659	.8838	.0105	.0105	.9818	.0031	.0104
.5649	.0016	.0016	.8850	.0175	.0175	.9868	.0018	.0044
.5681	.0016	.0016	.8873	.0296	.0296	.9868	.0026	.0056
.5681	.5313	.5313	.8873	.0035	.0035	.9878	.0020	.0044
.5697	.3625	.3625	.8899	.0035	.0035	.9878	.0017	.0042
.5697	.2369	.2369	.8899	.0251	.0251	.9890	.0006	.0031
.5826	.0840	.0840	.8935	.0251	.0251	.9925	.0010	.0035
.5846	.0760	.0760	.8935	.0004	.0011	.9925	.0005	.0013
.5863	.0480	.0480	.8955	.0004	.0011	.9941	.0004	.0007
.5988	.0311	.0311	.8955	.0052	.0111	.9961	.0002	.0004
.6045	.0258	.0258	.9157	.0035	.0106	1.0000	0	0

[a]Points of discontinuity in the EI/EI_{ref} function are recorded for their common x/L values.

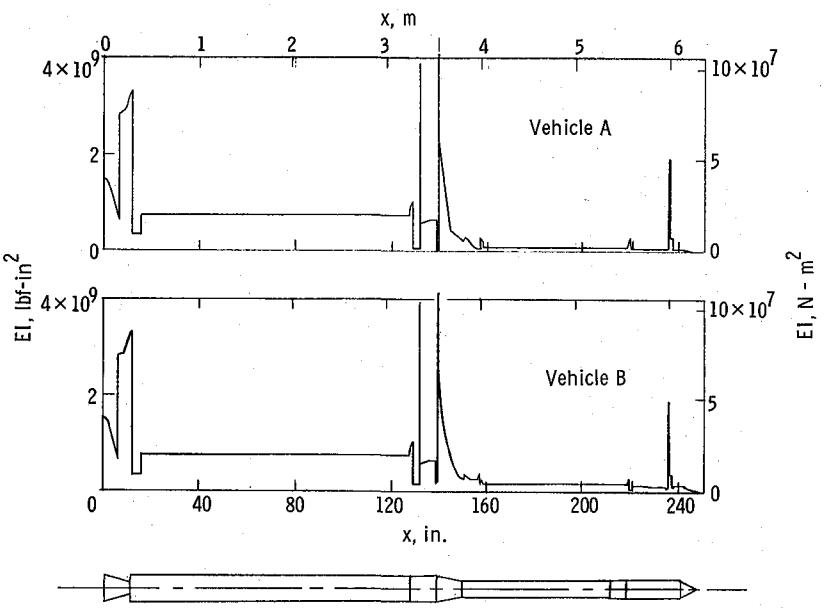

Figure 3.- Flexural-stiffness-coefficient distribution for vehicles A and B, including corrected distributions across structural joints. See table II for maximum value of EI at station 140.9 in. (3.579 m).

The stiffness data of table II and figure 3 include the equivalent stiffness distributions across structural joints. The estimated joint rotation constants used for computing the equivalent stiffness function are provided in table III. The structural joints description, classification, and approximate location on the vehicle are given in the table along with the estimated joint-rotation constants. The joint classifications and joint rotation constants were chosen from the joint data given in reference 7. The equivalent stiffness distributions across joints were approximated by the equivalent-stiffness formula given in reference 3.

TABLE III.- ESTIMATED JOINT ROTATION CONSTANTS

[$\kappa_{u_{ref}}$ = 100 × 10-9 rad/in-lbf (885.1 rad/m-N); L = 248.0 in. (6.299 m)]

Joint number	Joint description	Classification		x_u/L	$\kappa_u/\kappa_{u_{ref}}$	
		Vehicle A	Vehicle B		Vehicle A	Vehicle B
1	Nozzle-motor juncture, threaded	Good	Good	0.0609	0.08	0.08
2	Threaded transition section without butt	Moderate	Moderate	.5307	1.0	1.0
3	Threaded diaphragm	Good	Good	.5662	.5	.5
4	Nozzle-motor juncture, threaded	Good	Good	.6361	.3	.3
5	Threaded on inner sleeve	Good	Good	.8891	.3	.3
6	Lapped, screwed to inner ring	Moderate	Good	.8941	1.0	.4
7	Screwed to inner ring	Moderate	Moderate	.9519	1.0	1.0

The increase in flexural stiffness for vehicle B in comparison with vehicle A over the span $x/L = 0.6113$ to $x/L = 0.8838$ is due to the addition of a steel sleeve over the entire length of the second-stage motor. Also, improved joint construction provided a lower rotation constant and increased the stiffness over the span $x/L = 0.8935$ to $x/L = 0.8955$ for vehicle B. In addition, the use of better quality graphite over the span $x/L = 0.9548$ to $x/L = 1.0$ provided a further increase in stiffness values for vehicle B.

Verification of computed stiffness data.- In order to confirm that the computed stiffness distributions used in this investigation were representative for vehicles A and B, the following correlations were made:

(1) Correlation of computed undamped natural frequencies with those frequencies observed from flight telemetry records: It was felt that a comparison of computed natural frequencies in bending for vehicles A and B with the frequencies of lateral oscillations observed from flight telemetry records would provide a good check on the computation of the stiffness distributions of the vehicles if the mass distributions are assumed to be correct.

In reference 6 it was reported that the frequencies of oscillations observed just subsequent to launch for vehicles A and B were approximately 10 cps and 14 cps, respectively, and corresponded to the fundamental frequencies of the respective vehicles. A comparison of the calculated undamped first-mode frequencies, based upon the computed stiffness distributions, with those frequencies estimated from the telemetry records given in reference 6 show good agreement. Summarized results of these data comparisons are given in table IV.

TABLE IV.- A COMPARISON OF IN-FLIGHT FREQUENCIES OF OSCILLATION OBTAINED FROM TELEMETRY DATA WITH COMPUTED FIRST-MODE UNDAMPED NATURAL FREQUENCIES OF FREE-FREE VEHICLES

Vehicle	Flight data (ref. 6)		Computed data (method of ref. 8)	
	Time from launch, sec	Averaged frequency, cps	Time from launch, sec	Natural frequency, cps
A	0.25 to 0.75	≈10.5	0 to 1.0	10.5 to 10.9
B	0.36 to 0.90	≈13.9	0 to 1.0	12.3 to 13.0

The in-flight frequencies listed in table IV were obtained by averaging the frequencies measured from the accelerometer data over the indicated flight-observation period. The fundamental frequency of oscillation is not well defined from the telemetry data until a finite time after leaving the launcher (about 0.25 second) because of the presence of

launching disturbances. Also, the lateral accelerations are well decayed after approximately 1 second into the flight for both vehicles.

The natural frequencies were computed by the method of reference 8 by using the mass and stiffness data given in tables I and II, respectively. Secondary effects of shear deformation and rotary inertia were ignored; however, the effects on the first-mode frequency for the particular configurations are thought to be negligible. The acceptable frequency correlations support the applicability and confidence in the computed EI distributions for the full-length configurations.

(2) Correlation of measured and computed effective stiffness for the second stages of the two-stage A and B vehicle configurations: References 2 and 6 document results of static load tests which were used to estimate the structural stiffness of the second-stage motor and transition section for vehicles A and B. In these tests the configurations were loaded as a cantilevered structure in the approximate manner illustrated by the sketch in table V. The static-load tests reported in the references were made subsequent to the unsuccessful flight of vehicle A. Tests were performed on a second-stage structure, which was similar to vehicle A. This structure was stiffened in subsequent tests to obtain second-stage stiffness estimates for vehicle B.

The measurements obtained from the WRE static loads tests were used to estimate the elastic stiffnesses of the second-stage configurations through the application of simple beam theory. These stiffness values are defined as the load required to produce one degree of rotation at the aerodynamic center-of-pressure position of the nose cone-cylinder which is located ahead of the applied load point. (See sketch in table V.) The WRE stiffness values are given in table V.

TABLE V.- CORRELATION OF MEASURED AND COMPUTED EFFECTIVE STIFFNESS VALUES FOR SECOND STAGES OF TWO-STAGE A AND B VEHICLE CONFIGURATIONS

Sketch of static load test of second-stage motor and transition section

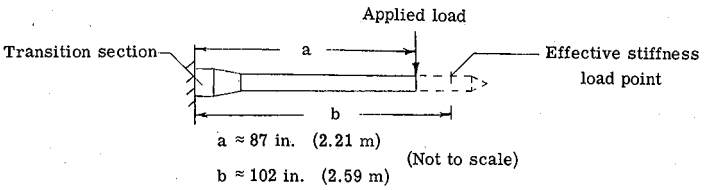

Vehicle	Measured stiffness (values from ref. 2)	Computed stiffness values[a]
A	200 lbf/deg (5.1×10^4 N/rad)	235 lbf/deg (5.99×10^4 N/rad)
B	400 lbf/deg (1.02×10^5 N/rad)	418 lbf/deg (1.07×10^5 N/rad)

[a]Computed by method of generating slope influence coefficients for a cantilever beam as given in reference 9. The stiffness values are valid for a load applied at the effective load point shown in the sketch, that is, approximately 102 in. (2.59 m) from the support.

An analysis was made for the purpose of computing slope influence coefficients for the cantilevered structures by using the calculated stiffness distributions for the second-stage structure and by comparing them with the estimated stiffness values. The slope influence coefficients were computed from a program applicable to cantilevered structures. (See ref. 9.) A comparison of the stiffness values given in table V shows that the computed stiffness values are only slightly larger than those estimated from the static tests. However, part of the disagreement may be related to the method of support. It is conceivable that a rotation could occur at the support, and thus give inaccurate stiffness measurements since an exact fixed-end boundary is often difficult to simulate. It is further evident that the stiffness analysis of the cantilevered structure requires an accurate definition of joint effects. For example, the test data of reference 6 indicate large reductions in structural stiffness in the joints at the forward end of the first-stage motor and at the separation diaphragm. These are the joints numbered 2 and 3 in table III. The behavior across the structural interfaces is difficult to predict but is approximated by joint rotation constants. The joint behavior is thought to contribute to the slight disagreement. However, the agreement between estimated (based on the WRE static load tests) and the computed stiffness values is considered to be very good in view of the many variables involved and tends to support the validity of the computed second-stage stiffness distributions.

Trajectory data.- The measured trajectory data provided by the Weapons Research Establishment include thrust, velocity, dynamic pressure, and Mach number. Their time-wise variation during first-stage boost are given in figures 4 for vehicles A and B.

Aerodynamic lift data.- The aerodynamic lift data used in the present analysis include the fin-body-combination lift data of figure 5 and the body-lift data given in figures 6 and 7.

The aerodynamic lift data presented in this paper includes that which was computed at the Langley Research Center for use in the analysis, and the supplementary data provided by the Weapons Research Establishment. The computed data are hereinafter referred to as LRC data, and the supplementary data are hereinafter designated as WRE data.

The total lift-force coefficients for the rigid fin-body combination as a function of Mach number are given in figure 5. The LRC data were computed by the methods of references 10 and 11. The carryover factors used in computing the LRC fin data are $K_{W(B)} = 1.25$ and $K_{B(W)} = 0.31$; the reference area is the effective planform area $S = 324$ in^2 (0.189 m^2). The lower dashed curve represents the fin data provided by WRE. The WRE data were calculated by the method of reference 2. The differences between the two curves in figure 5 are attributed to different estimates of the carryover

factors. The WRE data, unlike the LRC data, account for the variation in the carryover factors $\left(\text{primarily } K_{B(W)}\right)$ with Mach number.

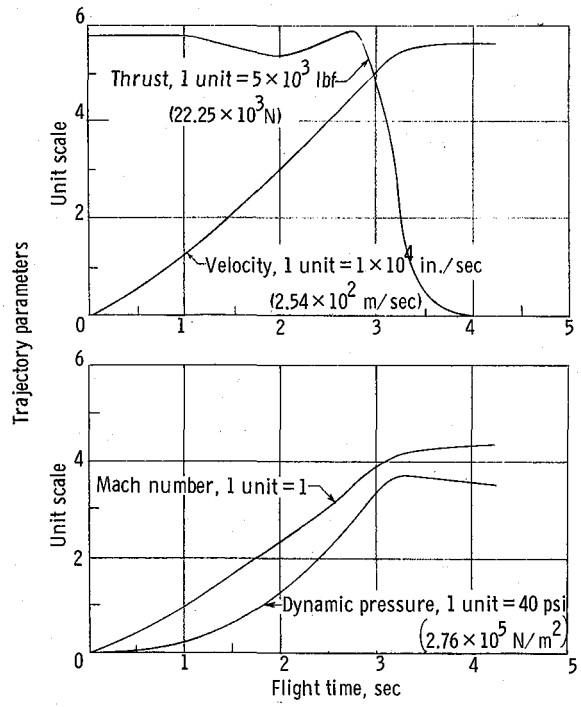

(a) Vehicle A.

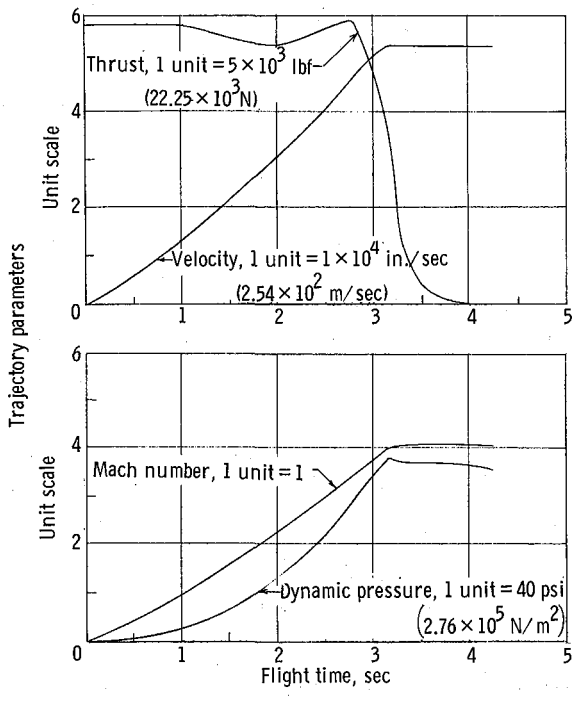

(b) Vehicle B.

Figure 4.- Trajectory parameters for vehicles A and B (thrust, velocity, Mach number, and dynamic pressure).

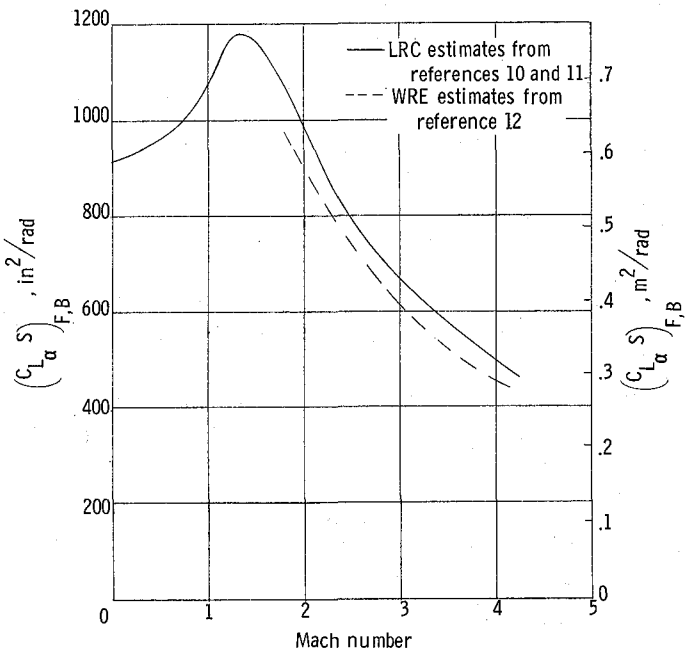

Figure 5.- Aerodynamic lift data applicable to vehicles A and B for the rigid fin-body combination. Data are given for effective lift of two panels in one plane, with respect to the three-panel fin arrangement.

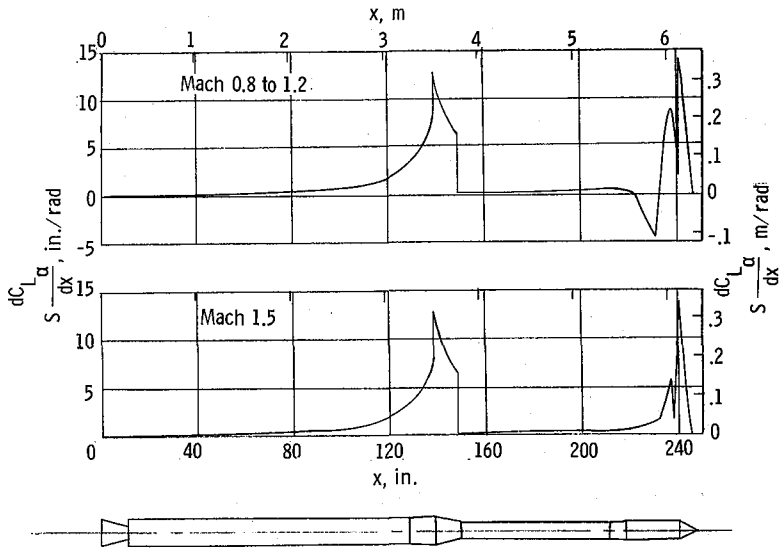

Figure 6.- LRC estimated body aerodynamic lift-force-coefficient slope distributions applicable to vehicles A and B at Mach numbers between 0.8 and 1.2 and at Mach 1.5.

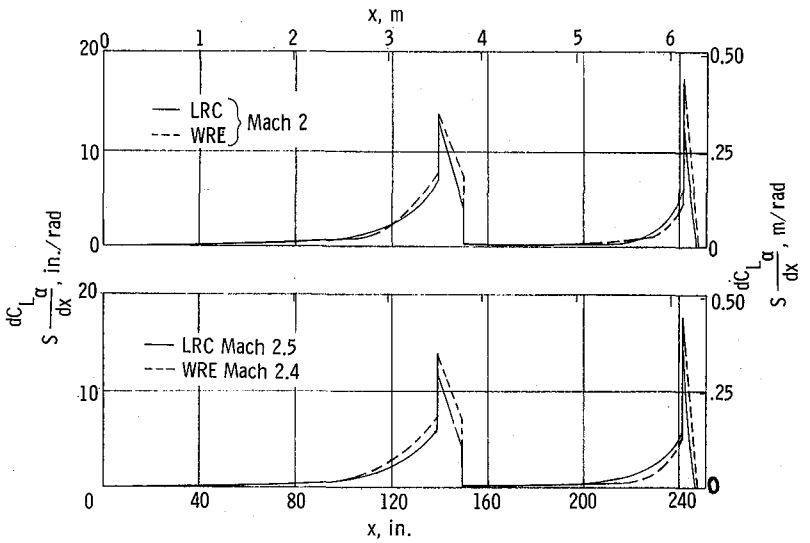

(a) Mach numbers 2.0, 2.4, and 2.5.

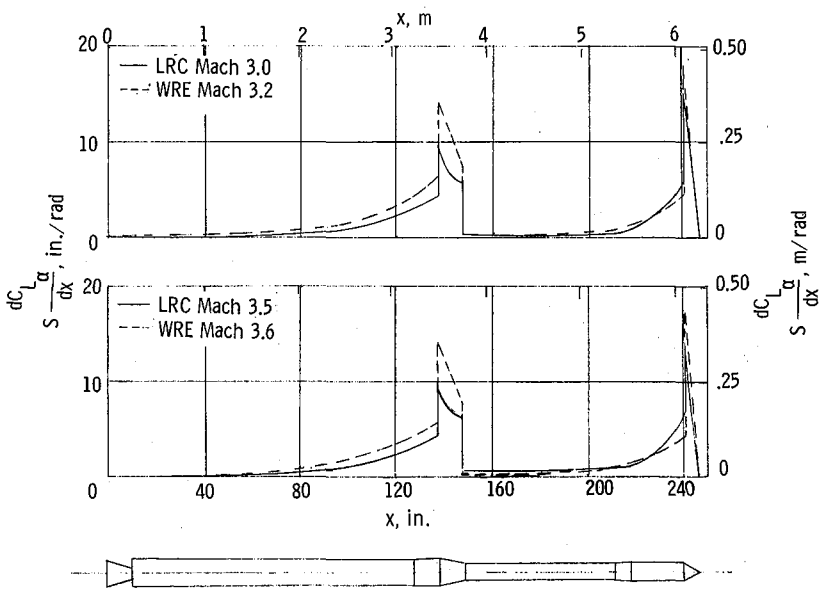

(b) Mach numbers 3.0, 3.2, 3.5, and 3.6.

Figure 7.- LRC and WRE estimated body aerodynamic lift-force-coefficient slope distributions applicable to vehicles A and B.

The computed body aerodynamic lift-force-coefficient slope distributions for various Mach numbers between 0.8 and 4.5 are given in figures 6 and 7. These distributions were calculated through the use of the digital computer program described in reference 13, which was used in conjunction with reference 14. The body aerodynamic lift-force-coefficient slopes furnished by the WRE for various Mach numbers between 2 and 4 are illustrated by the dashed curves in figures 7. The WRE data were derived from the methods of reference 15.

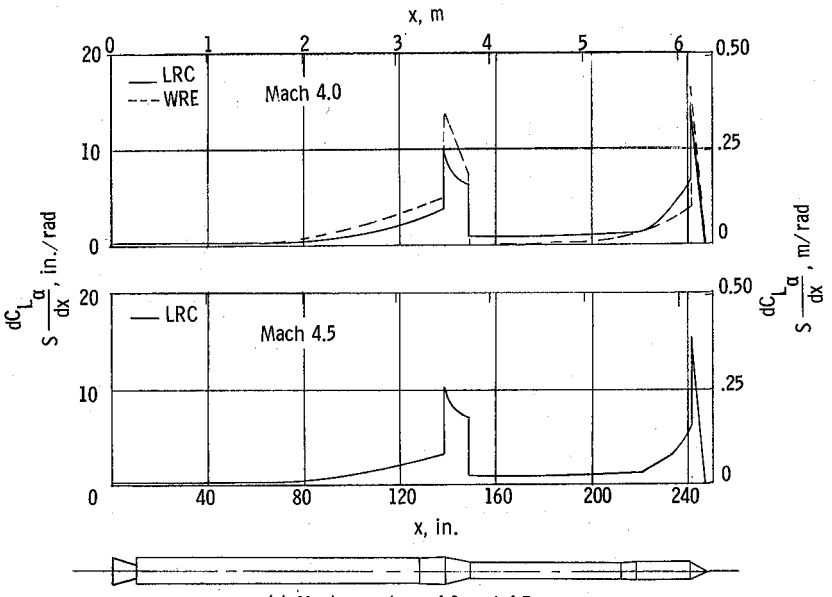

(c) Mach numbers 4.0 and 4.5.

Figure 7.- Concluded.

Comparisons between the LRC and the WRE body distributions show generally good agreement. The principal differences observed from the comparisons occur over the second-stage flare and first- to second-stage transition section at Mach numbers of 3 and greater. (See figs. 7(b) and 7(c).)

Aerodynamic drag data.- The distribution over the forebody of the drag-force-coefficient slopes that are used in the analysis are provided in figures 8 for various Mach numbers. These distributions were obtained from the data given in references 16 and 17 and are due to nonviscous aerodynamic loading only, exclusive of static pressures. Base drag influences are accounted for by corrections in the thrust levels.

Theoretical Aeroelastic Divergence Characteristics Compared With Flight Results

The pertinent divergence characteristics obtained from the applied analysis include the divergence dynamic pressure, generalized static margin for the flexible vehicle, and modal characteristics at divergence. Calculations were made at 12 points along the trajectory through first-stage burnout in order to obtain a good definition of the timewise variations in the computed divergence characteristics. The computations utilizing the WRE aerodynamic data, which were provided in the Mach number range 2 to 4 only, are restricted to flight times beyond 1.75 seconds.

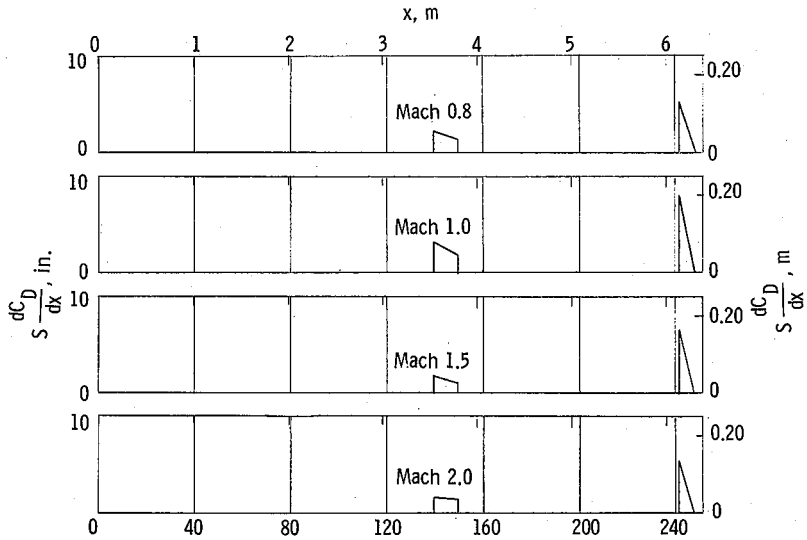

(a) Mach numbers 0.8, 1.0, 1.5, and 2.0.

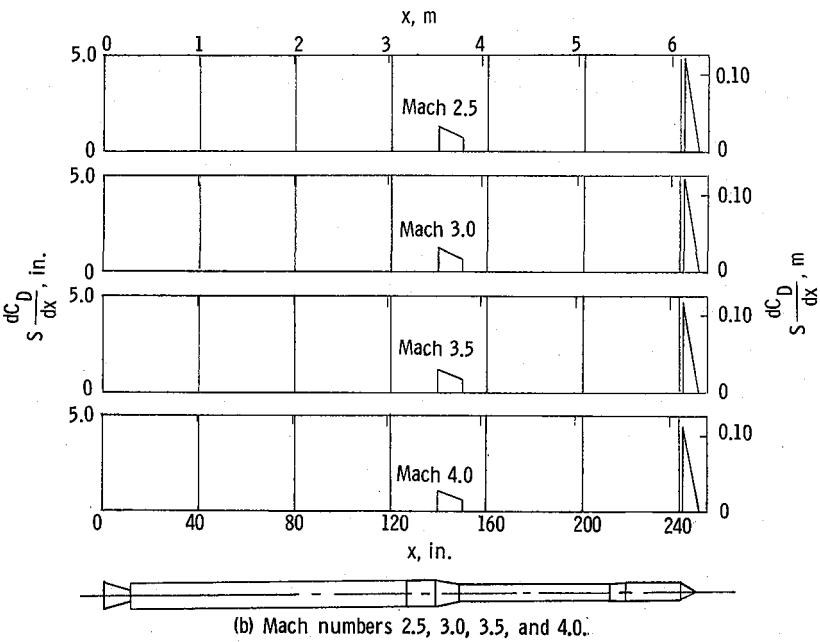

(b) Mach numbers 2.5, 3.0, 3.5, and 4.0.

Figure 8.- Estimated forebody drag-force-coefficient distributions applicable to vehicles A and B.

Computed divergence boundary, q_{div}.- The timewise variations in the computed dynamic pressure of divergence (based upon LRC aerodynamic data) and the actual flight dynamic pressure for vehicles A and B, respectively, are illustrated in figures 9. The data of figure 9(a) show the vehicle A penetrating the theoretical divergence boundary at very near the actual time of failure. An iteration procedure, which is discussed under the section entitled "Method of Analysis," was used to compute the divergence condition

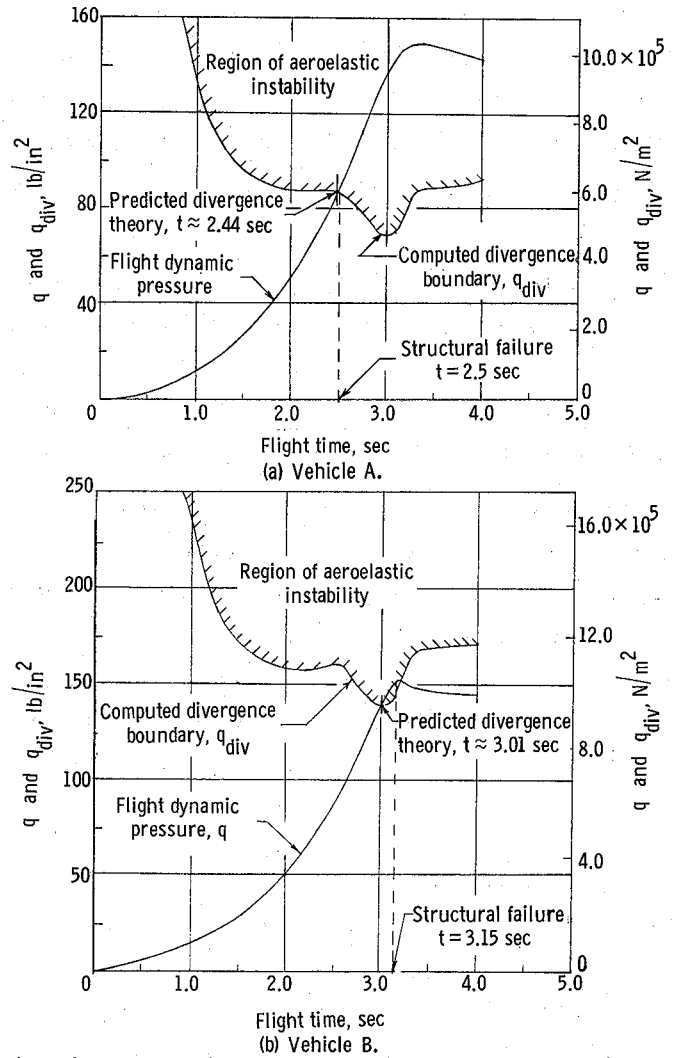

Figure 9.- Computed divergence boundary (based on LRC aerodynamic data) and actual flight dynamic pressure profile.

compatible with the actual trajectory and LRC input data. This procedure established the theoretical divergence condition at $t \approx 2.44$ seconds. After this time, the vehicle is operating beyond the theoretical divergence boundary, as illustrated in the figure.

The data of figure 9(b) applies to the stiffened vehicle B and also shows the divergence boundary penetration to occur near the actual time of failure. The iterated condition of aeroelastic divergence that is compatible with the actual flight trajectory is computed to occur at $t \approx 3.01$ seconds which is the first intercept of the q-curves with the boundary in figure 9(b). The curves in figure 9(b) show the vehicle B to be operating within the region of divergence for only a short period of time (approximately 0.20 second); however, it did not recover and structural failure coincided with the time of maximum dynamic pressure.

The results given in figures 9 reveal good agreement between the theoretical condition of aeroelastic divergence and actual failure times for both vehicles. These comparisons are made on the assumption that failure will occur upon penetration of the divergence boundary. In both cases the method gives only slightly conservative results; that is, structural failure occurs just subsequent to predicted divergence. On a timewise basis, the time lapses are only 0.06 second and 0.14 second for vehicles A and B, respectively.

A comparison of the theoretical divergence times with the observed times at which divergence began to occur, as was discussed under "Vehicles Description and Flight Behavior" shows the agreement in time to be 0.02 second (later) for vehicle A and 0.00 second for vehicle B. This comparison indicates a highly accurate agreement on the onset of divergence, structure failure occurring just subsequently.

Computed aeroelastic stability measures.- The aeroelastic divergence correlations can also be observed in terms of the aeroelastic stability measures discussed under "Method of Analysis." The computed aeroelastic stability measures in terms of the dynamic pressure ratio q/q_{div} and the generalized static margin parameter variations with flight time based on both LRC and WRE aerodynamic data are given in figure 10. The solid curves pertain to the results obtained by using LRC aerodynamic data whereas the dashed curves are based upon the use of the WRE aerodynamic data.

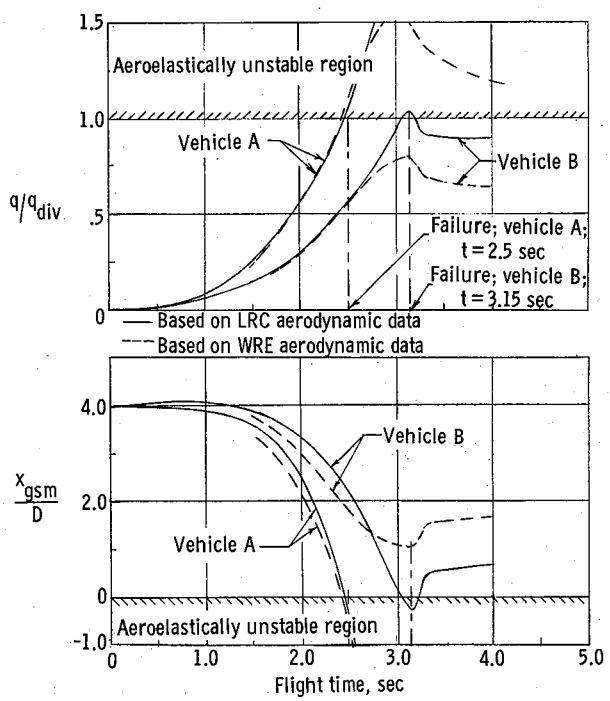

Figure 10.- Computed aeroelastic stability characteristics for vehicles A and B. D = 10 in. (0.254 m).

The solid curves in the upper graph of figure 10 are derived from the data of figures 9 from the ratio of the actual flight dynamic pressure q to the theoretical divergence boundary q_{div}. The computed stability indices q/q_{div} at actual failure, respectively, for vehicles A and B are computed to be 1.03 and 1.04. The computed stability indices greater than unity reflect the aforementioned results on divergence predictions in terms of the percentage of flight q above the computed divergence boundary q_{div} at the time of failures. Also, it is interesting to note that stability indices at failure for the LRC cases are almost identical. However, this is not true for the results obtained when the WRE aerodynamic data are used.

The analysis using the WRE aerodynamic data gave interesting results. For the WRE data, the computed q/q_{div} ratios at times of failure were found to be 1.08 and 0.78 for vehicles A and B, respectively. The results for vehicle A at divergence are seen to be only slightly more conservative than the LRC result but are much less conservative for vehicle B. The stability index of $q/q_{div} = 0.78$ at the condition of maximum dynamic pressure for vehicle B suggests the possibility of a successful flight. However, it should be apparent that the vehicle was operating too near the divergence boundary and far above the criterion suggested in reference 5, namely, that the maximum operating dynamic pressure should not be greater than one-half the boundary value, that is $q \leq 0.5q_{div}$. The reason for the slightly more conservative predictions for vehicle A when WRE data are used is attributed to differences in fin-lift estimates and the less conservative predictions for vehicle B can be traced to considerable differences in the forebody aerodynamic lift distributions at the high Mach number, particularly over the first- to second-stage transition section. The differences in the LRC and WRE body-lift distributions at Mach 4 may be seen by comparing the distributions in the upper graph in figure 7(c).

The variations in the calculated generalized static margin parameter x_{gsm}/D with flight time are illustrated in the lower graph in figure 10. The generalized static margin curves reflect the same aeroelastic behavior that is illustrated in the upper graph. For example, the generalized static margin parameter curves give the same boundary penetration time as the q/q_{div} curves, that is $x_{gsm}/D = 0$, when $q/q_{div} = 1.0$ which is the theoretical condition of aeroelastic instability. The use of the generalized static margin parameter provides a theoretical shift in the aerodynamic center of pressure due to aeroelastic effects and is sometimes preferred when stability evaluations are desired from a static margin viewpoint.

Computed aeroelastic divergence mode shapes.- The computed divergence mode shapes at times of predicted failure for vehicles A and B are given in figure 11. The vehicle shapes in the divergence mode are illustrated in the figure by superimposing the deformed configuration outline onto the computed mode shape and are shown in relation to the rigid vehicle outline having the same normalized angle of attack at $x = 0$. The

mode shapes are shown with respect to the velocity-axis system and the vertical scale is exaggerated for the purpose of illustration.

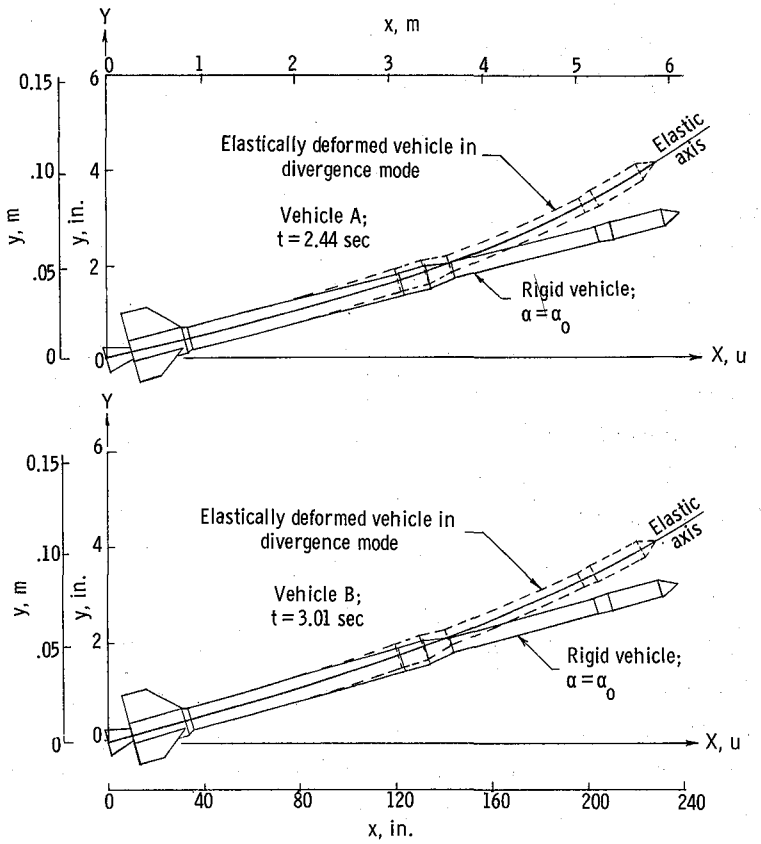

Figure 11.- Illustration of elastically deformed vehicle configurations at times of predicted aeroelastic divergence. Normalized for a chosen value of $R = 1.0 \times 10^6$ in. (2.54×10^4 m).

The aeroelastic bending of both vehicles A and B is characterized by appreciable deformation beginning near the forward end of the first-stage motor and increasing toward the forward end of the vehicle, relatively large changes in the local slope occurring over the transition section and the second-stage motor.

The characteristic divergence mode shapes reveal that the aeroelastic instabilities resulting in structural failure for both vehicles were due largely, but not entirely, to the second-stage configuration flexibility. A close comparison of the mode shapes with respect to the rigid configurations indicate only slightly less bending over the second stage of vehicle B; otherwise, the mode shapes are almost identical. The effect of stiffening the second stage of vehicle B is apparent in that the mode shape at divergence, which has the same characteristics as that of vehicle A, is associated with a much higher dynamic pressure. However, the comparisons are not exact since the loads distribution

and trajectory characteristics are different at the separate conditions of predicted divergence.

Rigid-Vehicle Stability Characteristics

The static margin, aerodynamic center-of-pressure and center-of-gravity data for the assumed rigid vehicle are essential to a complete stability evaluation. These data are graphically displayed in figure 12 for both vehicles.

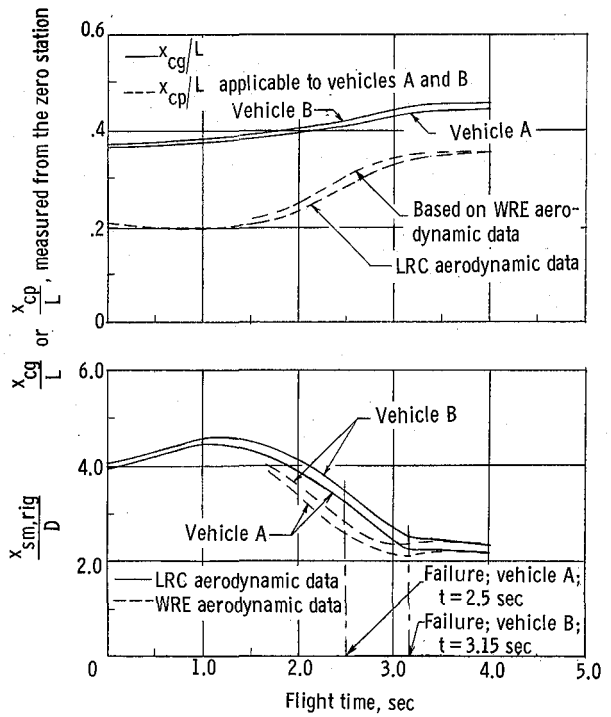

Figure 12.- Computed center-of-gravity, aerodynamic center-of-pressure, and static margin characteristics for the rigid vehicles. L = 248 in. (6.299 m); D = 10.0 in. (0.254 m).

In the upper graph of figure 12 the timewise variations in the computed center of gravity and static aerodynamic center of pressure are illustrated. The difference in the center-of-gravity locations for vehicles A and B is primarily due to the previously mentioned addition of a steel stiffening sleeve over the second stage of vehicle B, which shifts the mass center slightly forward. The differences observed between the LRC and WRE static aerodynamic centers of pressures are primarily due to the difference in fin-lift estimates and secondarily due to differences in body-lift estimates.

The computed rigid-vehicle static margin variations with flight time are given in the lower graph of figure 12. Note that the minimum rigid-vehicle static margin for either of the two vehicles utilizing both sets of aerodynamic data is greater than two body

diameters throughout first-stage flight. This observation emphasizes a very important point, namely, that the stability of slender launch vehicles cannot be evaluated by the rigid-body static margin parameter alone. For example, the controlling rigid-body static margin criterion for these vehicles is 1 maximum body diameter, based upon the criterion suggested in reference 5. If the static stability for these vehicles were evaluated on the basis of this criterion alone, the design would seem to be adequate. Rigid-body static margins, based on LRC data, are computed to be 3.3 and 2.5 body diameters for vehicles A and B, respectively, at the times of failure; however, at these times the aerodynamic centers of pressures have shifted forward because of aeroelastic deformation, and instability and structural failures result.

Method Evaluation

In the foregoing discussion, data have been presented which reveal good correlation between the theoretical divergence predictions and the actual flight results.

Although the investigation is limited to the analysis of only two flight failures, the results provide good support to the adequacy of the theoretical technique of reference 3. Also, the fact that the method has predicted freedom from aeroelastic instabilities for approximately seven different launch vehicles which have been flown successfully lends further support to the adequacy of the method.

This investigation verifies the previous conclusions by WRE that vehicles A and B failed because of aeroelastic divergence. The present analysis also indicates the importance of strict adherence to accepted aeroelastic stability criteria in the aeroelastic design evaluation of unguided launch vehicles.

CONCLUDING REMARKS

An analysis is presented for two experimental launch vehicles which are known to have failed because of aeroelastic divergence. The input data for the analysis are provided along with the computed aeroelastic divergence data. The correlation and verification of the stiffness levels of the vehicles are presented along with the results of the theoretical analysis utilizing two different sets of aerodynamic data.

The correlation of theoretical aeroelastic divergence characteristics with flight data gives very good agreement between the actual and predicted conditions of aeroelastic divergence leading to structural failure.

Static-margin data based on rigid-vehicle considerations are included to illustrate the fallacy of basing the stability evaluation of unguided slender, launch vehicles upon the rigid-vehicle static margin parameter alone.

Based upon results of this investigation, the theoretical method of NASA Technical Note D-3893 appears to be adequate for predicting aeroelastic divergence and for evaluating the design of unguided, flexible launch vehicles in view of their aeroelastic divergence characteristics.

Langley Research Center,
National Aeronautics and Space Administration,
Langley Station, Hampton, Va., February 7, 1968,
124-08-05-25-23.

REFERENCES

1. Arbic, Richard G.; White, George; and Gillespie, Warren, Jr.: Some Approximate Methods for Estimating the Effects of Aeroelastic Bending of Rocket-Propelled Model-Booster Combinations. NACA RM L53A08, 1953.

2. Thomson, K. D.: The Aero-Elastic Divergence of Slender Multi-Stage Test Vehicles. Tech. Note HSA 93, Weapons Res. Estab., Australian Dep. of Supply, Nov. 1962.

3. Young, Clarence P., Jr.: A Numerical Method for Determining the Aeroelastic Divergence Characteristics of Unguided, Slender-Body, Multistage Launch Vehicles. NASA TN D-3893, 1967.

4. Mechtly, E. A.: The International System of Units – Physical Constants and Conversion Factors. NASA SP-7012, 1964.

5. Alley, Vernon L., Jr.; and Gerringer, A. Harper: An Analysis of Aeroelastic Divergence in Unguided Launch Vehicles. NASA TN D-3281, 1966.

6. Thomson, K. D.: Analysis of Jabiru Firings Nos. 901 and 904. Tech. Memo. No. HSA 66, Weapons Res. Estab., Australian Dep. of Supply, Oct. 1959.

7. Leadbetter, Sumner, A.; Alley, Vernon L., Jr.; Herr, Robert W.; and Gerringer, A. Harper: An Experimental and Analytical Investigation of the Natural Frequencies and Mode Shapes of a Four-Stage Solid-Propellant Rocket Vehicle. NASA TN D-1354, 1962.

8. Alley, Vernon L., Jr.; Guillotte, Robert J.; and Hunter, Lessie D.: A Method of Determining Modal Data of a Nonuniform Beam With Effects of Shear Deformation and Rotary Inertia. NASA TN D-2930, 1965.

9. Alley, Vernon L., Jr.; and Gerringer, A. Harper: A Matrix Method for the Determination of the Natural Vibrations of Free-Free Unsymmetrical Beams With Application to Launch Vehicles. NASA TN D-1247, 1962.

10. Pitts, William C.; Nielsen, Jack N.; and Kaattari, George E.: Lift and Center of Pressure of Wing-Body-Tail Combinations at Subsonic, Transonic, and Supersonic Speeds. NACA Rep. 1307, 1957.

11. Anon.: USAF Stability and Control Datcom. Contracts AF 33(616)-6460 and AF 33(615)-1605, Douglas Aircraft Co., Inc., Oct. 1960, Revised Nov. 1965.

12. Stanbrook, A.: The Lift-Curve Slope and Aerodynamic Centre Position of Wings at Subsonic and Supersonic Speeds. Tech. Note No. Aero.2328, Brit. R.A.E., Nov. 1954.

13. Madden, Ragan B.: Computing Program for Axial Distribution of Aerodynamic Normal-Force Characteristics for Axisymmetric Multistage Launch Vehicles. NASA TN D-4342, 1968.

14. Muraca, Ralph J.: An Empirical Method for Determining Static Distributed Aerodynamic Loads on Axisymmetric Multistage Launch Vehicles. NASA TN D-3283, 1966.

15. Phythian, J. E.; and Dommett, R. L.: Semi-Empirical Methods for Estimating Forces on Bodies at Supersonic Speeds. J. Roy. Aeron. Soc., vol. 62, no. 571, July 1958, pp. 520-524.

16. Sims, Joseph L.: Tables for Supersonic Flow Around Right Circular Cones at Zero Angle of Attack. NASA SP-3004, 1964.

17. Johnson, Benford H.; and Hamner, Roger L.: A Summary of the Trisonic Cone-Cylinder Aerodynamic Loads Study. Rep. LMSC/HREC A712618 (Contract NAS 8-11289), Lockheed Missiles & Space Co., Nov. 30, 1965.

NASA-Langley, 1968 —— 32 L-5752

NATIONAL AERONAUTICS AND SPACE ADMINISTRATION
WASHINGTON, D. C. 20546

OFFICIAL BUSINESS

FIRST CLASS MAIL

POSTAGE AND FEES PAID
NATIONAL AERONAUTICS AND
SPACE ADMINISTRATION

POSTMASTER: If Undeliverable (Section 158 Postal Manual) Do Not Return

"The aeronautical and space activities of the United States shall be conducted so as to contribute . . . to the expansion of human knowledge of phenomena in the atmosphere and space. The Administration shall provide for the widest practicable and appropriate dissemination of information concerning its activities and the results thereof."

—NATIONAL AERONAUTICS AND SPACE ACT OF 1958

NASA SCIENTIFIC AND TECHNICAL PUBLICATIONS

TECHNICAL REPORTS: Scientific and technical information considered important, complete, and a lasting contribution to existing knowledge.

TECHNICAL NOTES: Information less broad in scope but nevertheless of importance as a contribution to existing knowledge.

TECHNICAL MEMORANDUMS: Information receiving limited distribution because of preliminary data, security classification, or other reasons.

CONTRACTOR REPORTS: Scientific and technical information generated under a NASA contract or grant and considered an important contribution to existing knowledge.

TECHNICAL TRANSLATIONS: Information published in a foreign language considered to merit NASA distribution in English.

SPECIAL PUBLICATIONS: Information derived from or of value to NASA activities. Publications include conference proceedings, monographs, data compilations, handbooks, sourcebooks, and special bibliographies.

TECHNOLOGY UTILIZATION PUBLICATIONS: Information on technology used by NASA that may be of particular interest in commercial and other non-aerospace applications. Publications include Tech Briefs, Technology Utilization Reports and Notes, and Technology Surveys.

Details on the availability of these publications may be obtained from:

SCIENTIFIC AND TECHNICAL INFORMATION DIVISION

NATIONAL AERONAUTICS AND SPACE ADMINISTRATION

Washington, D.C. 20546